THE JOURNAL OF PHYSICAL CHEMISTRY LETTERS
A JOURNAL OF THE AMERICAN CHEMICAL SOCIETY

pubs.acs.org/JPCL

Letter

Unraveling How Multivalency Triggers Shape Deformation of Sub-100 nm Lipid Vesicles

Hyeonjin Park,[§] Tun Naw Sut,[§] Bo Kyeong Yoon, Vladimir P. Zhdanov, Nam-Joon Cho,* and Joshua A. Jackman*

Cite This: *J. Phys. Chem. Lett.* 2021, 12, 6722–6729

Read Online

ACCESS | Metrics & More | Article Recommendations | Supporting Information

ABSTRACT: Multivalent ligand–receptor interactions are critical to the function of membrane-enveloped biological and biomimetic nanoparticles, yet resulting nanoparticle shape changes are rarely investigated. Using the localized surface plasmon resonance (LSPR) sensing technique, we tracked the attachment of biotinylated, sub-100 nm lipid vesicles to a streptavidin-functionalized supported lipid bilayer (SLB) and developed an analytical model to extract quantitative details about the vesicle–SLB contact region. The experimental results were supported by theoretical analyses of biotin–streptavidin complex formation and corresponding structural and energetic aspects of vesicle deformation. Our findings reveal how varying the surface densities of streptavidin receptors in the SLB and biotin ligands in the vesicles affects the extent of nanometer-scale vesicle deformation. We also identify conditions, i.e., a critical ligand density, at which appreciable vesicle deformation began, which provides insight into how the membrane bending energy partially counterposes the multivalent binding interaction energy. These findings are generalizable to various multivalent ligand–receptor systems.

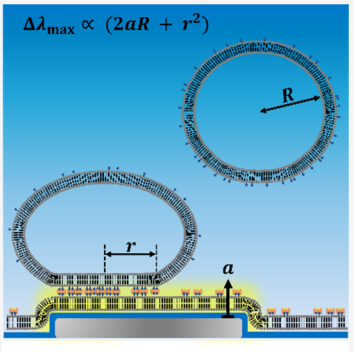

Multivalent binding interactions are widely found in biological systems,[1−3] and well-known examples involving biological nanoparticles include virion and exosome attachment to cellular membrane interfaces.[4−9] These interactions can have significant biomedical implications, such as affecting the degree of virus transmissibility (see, e.g., refs 10 and 11), and have also inspired the biomimetic design of therapeutic and diagnostic nanoparticles and tools based on receptor mimicking.[12−16] While multivalent ligand–receptor interactions have been extensively studied in the context of biological nanoparticle attachment,[17−20] an emerging and less well understood topic concerns the resulting shape changes of attached nanoparticles[21,22] (see also discussion in refs 23 and 24). When soft-matter biological and biomimetic nanoparticles such as membrane-enveloped virions, exosomes, and lipid vesicles attach to a receptor-functionalized surface, they can, in principle, undergo deformation that is dictated by the balance of the multivalent binding interaction and membrane bending energies[25−30] (see also examples of shape changes in the receptor-functionalized surface itself[31−33]). In cases of mobile ligands and receptors, the deformation process can be accompanied by the redistribution of ligands and receptors, effectively increasing their concentrations within the contact region.

To date, most studies have treated the attaching biological nanoparticles as nondeformable, while exploring cases that involve deformable nanoparticles and reshaping events is relevant to various biological applications. For example, using the quartz crystal microbalance-dissipation (QCM-D) technique, a recent study[34] tracked the attachment of biotinylated, ∼100 nm diameter vesicles to a cell-membrane-mimicking, streptavidin-protein-functionalized supported lipid bilayer (SLB) platform[35,36] and reported a transition in the structural properties of attached vesicles depending on the fraction of biotinylated lipids in the vesicles. However, it was not possible to extract quantitative shape or energy information about the implied deformation of attached vesicles due to the relatively long penetration depth (∼100 nm) and hydrodynamic coupling effects associated with the QCM-D technique.[37] In principle, ligand–receptor interactions involving ligand-presenting nanoparticles can also be scrutinized by atomic force microscopy (AFM), but again there are technical challenges such as probe-related artifacts, low throughput, and hindered access to the nanoparticle–surface contact region.[38] All of these limitations motivate utilizing other classes of ensemble-average bioanalytical sensors, especially nanoplasmonic sensing techniques, that have higher surface sensitivity (shorter penetration depth) and can detect mass and conformational changes associated with biomacromolecular mass only.[39]

Herein, we conducted localized surface plasmon resonance (LSPR) sensing experiments to track the attachment of biotinylated, fluid-phase lipid vesicles onto streptavidin-

Received: May 11, 2021
Accepted: July 12, 2021

https://doi.org/10.1021/acs.jpclett.1c01510
J. Phys. Chem. Lett. 2021, 12, 6722–6729

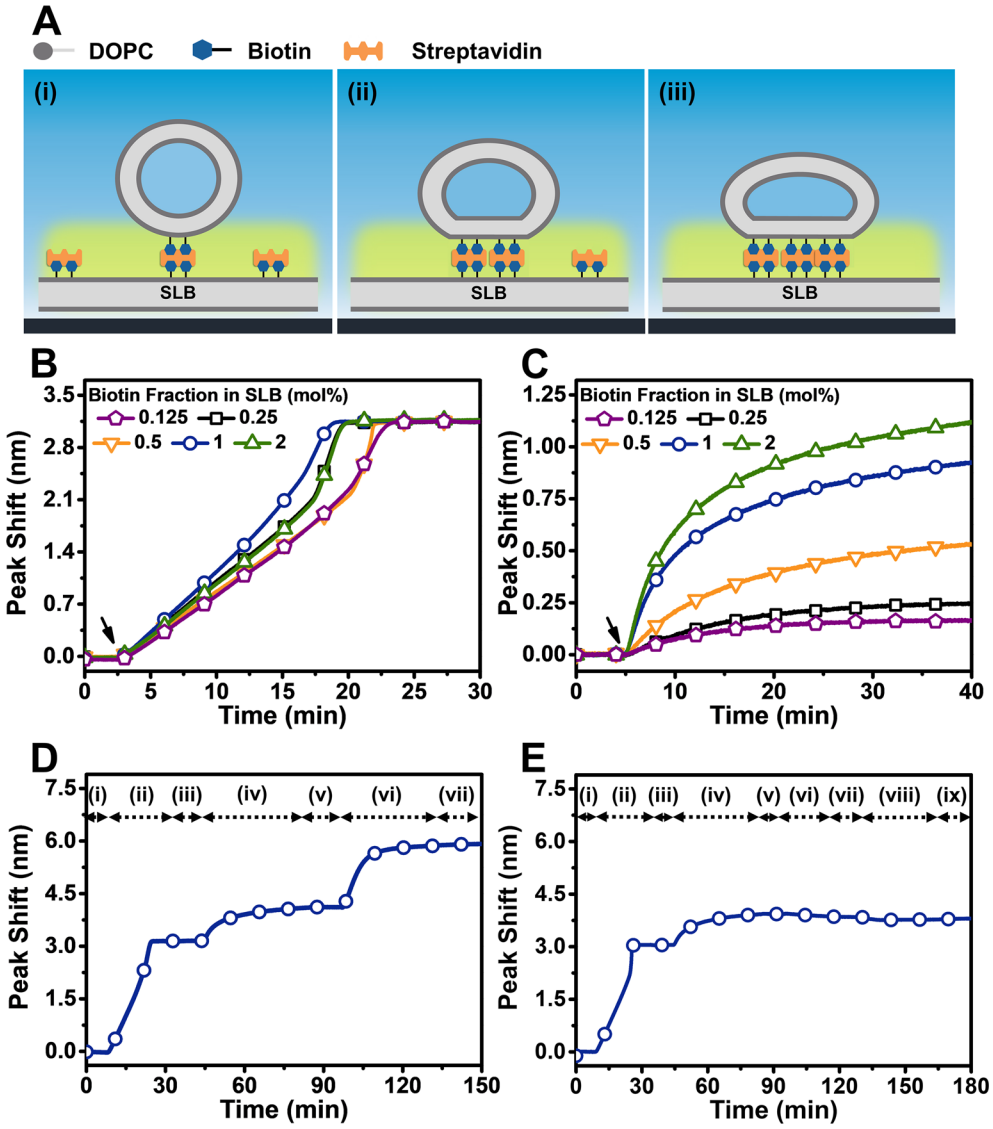

Figure 1. Experimental strategy and SLB platform fabrication. (A) Schematic illustration of LSPR measurement approach to track biotinylated lipid vesicle attachment onto a streptavidin-functionalized SLB platform. For example, we show the situation when the biotin fraction in the SLB is in excess compared to that in vesicles. A larger number of biotin−streptavidin binding events can increase the multivalent binding interaction energy, which translates into greater deformation of attached vesicles, and hence, lipid molecules are, on average, closer to the sensor surface and in a region of higher LSPR-enhanced electromagnetic field intensity. (B) Time-resolved $\Delta\lambda_{max}$ shifts during SLB formation on silica-coated sensor surfaces. The baselines correspond to buffer solution, and DOPC/DOPE-biotin lipid bicelles were added starting at t = 3 min. (C) Time-resolved $\Delta\lambda_{max}$ shifts for streptavidin-binding to SLBs with different biotin fractions. The baselines correspond to the SLBs in buffer solution, and streptavidin was added starting at around t = 5 min. (D) Step-by-step $\Delta\lambda_{max}$ shift responses for (i) buffer baseline, (ii) SLB formation, (iii) buffer washing, (iv) streptavidin addition, (v) buffer washing, (vi) vesicle addition, and (vii) buffer washing. (E) Step-by-step $\Delta\lambda_{max}$ shift responses for control experiment. Steps i−v were the same as in panel D, followed by (vi) free biotin addition, (vii) buffer washing, (viii) vesicle addition, and (ix) buffer washing.

functionalized biotinylated SLBs (Figure 1A). To clarify the aforementioned specifics of the multivalent interactions in this generic system, we systematically varied the biotin fraction in the SLB (in turn, modulating the surface density of streptavidin receptors) and the biotin ligand fraction in the vesicles and scrutinized the LSPR measurement responses at saturation and corresponding attachment kinetics. Compared to the QCM-D and surface plasmon resonance (SPR) techniques, the LSPR technique has a much shorter penetration depth on the order of 5−20 nm (refs 40 and 41) and is sensitive to changes in the local refractive index, which is ideal for probing the receptor-mediated deformation of attached, sub-100 nm vesicles, and related structural and energetic aspects because deformation in such cases takes place primarily in the contact region near the sensor surface on a length scale that is comparable to the LSPR penetration depth.

Our measurement platform consisted of a streptavidin-functionalized SLB on top of a silica-coated silver nanodisk array,[42] and vesicle attachment kinetics were tracked by monitoring a shift in the maximum-intensity extinction wavelength, $\Delta\lambda_{max}$, of the embedded plasmonic nanodisk transducers.[43] First, we fabricated biotinylated SLB platforms via the bicelle method,[44] and LSPR measurements verified SLB formation on account of two-step accelerating kinetics and final $\Delta\lambda_{max}$ shifts around 3.11 ± 0.05 nm (Figure 1B). The resulting SLBs contained mainly 1,2-dioleoyl-*sn*-glycero-3-

https://doi.org/10.1021/acs.jpclett.1c01510
J. Phys. Chem. Lett. 2021, 12, 6722−6729

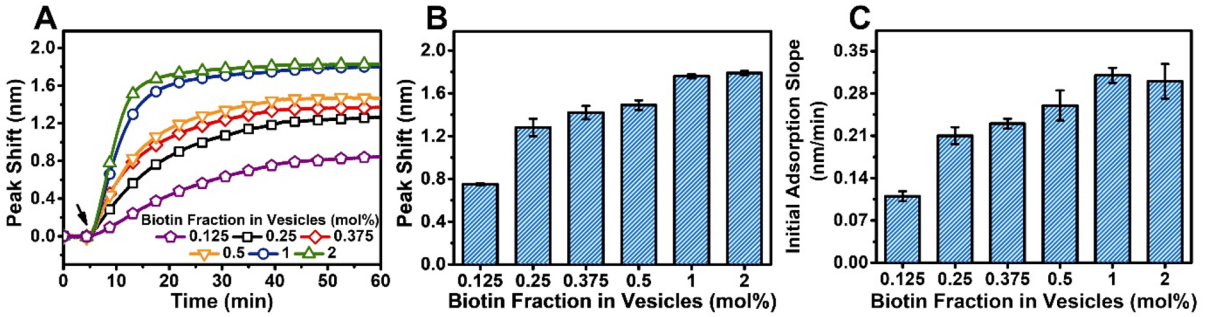

Figure 2. LSPR tracking of biotin-mediated vesicle attachment to streptavidin-functionalized SLBs with varying biotin fractions in the vesicles. The biotin fraction in the vesicles ranged from 0.125 to 2 mol %, and the streptavidin-coated SLB contained 1 mol % biotin. (A) Time-resolved $\Delta\lambda_{max}$ shifts during vesicle attachment. The baseline corresponds to the streptavidin-functionalized SLB, and the vesicles were added starting at t = 5 min, followed by buffer washing from t = 40 min. (B) Summary of final $\Delta\lambda_{max}$ shifts after buffer washing. (C) Summary of the initial rate of change in the λ_{max} signal. For panels B and C, the data are reported as the mean ± standard deviation from three measurement runs.

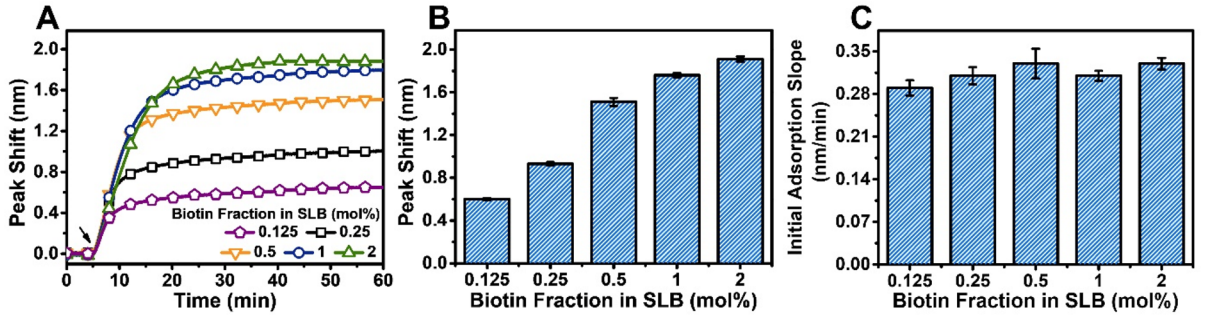

Figure 3. LSPR tracking of biotin-mediated vesicle attachment to streptavidin-functionalized SLBs with varying biotin fractions in the SLB. The biotin fraction in the SLB ranged from 0.125 to 2 mol %, and the biotin fraction in the vesicles was fixed at 1 mol %. (A) Time-resolved $\Delta\lambda_{max}$ shifts during vesicle attachment. The baseline corresponds to the streptavidin-functionalized SLB, and the vesicles were added starting at t = 5 min, followed by buffer washing from t = 40 min. (B) Summary of final $\Delta\lambda_{max}$ shifts after buffer washing. (C) Summary of the initial rate of change in the λ_{max} signal. For panels B and C, the data are reported as the mean ± standard deviation from three measurement runs.

phosphocholine (DOPC) lipid and a small fraction of 1,2-dioleoyl-*sn*-glycero-3-phosphoethanolamine-N-(cap biotinyl) (DOPE-biotin) lipid (0−2 mol %) that was tuned according to the bicelle composition. In turn, the degree of streptavidin protein binding to the SLBs depended on the biotinylated lipid fraction[45] within an SLB, and the corresponding $\Delta\lambda_{max}$ shifts varied from 0.17 ± 0.01 to 1.14 ± 0.03 nm as the biotin fraction increased from 0.125 to 2 mol % (Figure 1C).

Figure 1D shows a representative example of an entire LSPR measurement run in which case a biotinylated SLB was formed, followed by streptavidin binding and subsequent addition of biotinylated lipid vesicles under flow conditions. Appreciable $\Delta\lambda_{max}$ shifts occurred at each step, and the results are indicative of vesicle attachment. In a control experiment, we incubated free biotin molecules with a streptavidin-functionalized SLB prior to adding the biotinylated lipid vesicles; in that case, no subsequent vesicle attachment was observed (Figure 1E). It was also verified that no vesicle attachment occurred when either the SLB or vesicles did not contain biotinylated lipids (Figure S1). These results verified that vesicle attachment is mediated by streptavidin protein receptors, and all stages of platform fabrication were also confirmed by QCM-D experiments (Figures S2−S4). In the following data sets, the initial baselines in the LSPR measurements correspond to the streptavidin-functionalized SLB platform and the reported $\Delta\lambda_{max}$ shifts correspond to the vesicle addition step.

Figure 2A presents the time-resolved $\Delta\lambda_{max}$ shifts for tracking vesicle attachment onto a streptavidin-functionalized SLB with 1 mol % biotin, and the tested vesicle populations had different biotin fractions (0.125−2 mol %). In all cases, monotonic attachment occurred until saturation, and the final $\Delta\lambda_{max}$ shifts were generally larger for vesicles with greater biotin fractions. For vesicles with 0.125 mol % biotin, the final $\Delta\lambda_{max}$ shift at saturation was 0.75 ± 0.01 nm, while the $\Delta\lambda_{max}$ shift increased to 1.28 ± 0.08 nm for vesicles with 0.25 mol % biotin (Figure 2B). For vesicles with 0.375 and 0.5 mol % biotin, the corresponding $\Delta\lambda_{max}$ shifts were 1.42 ± 0.06 and 1.49 ± 0.04 nm, respectively. On the other hand, for vesicles with 1 and 2 mol % biotin fractions, the corresponding $\Delta\lambda_{max}$ shifts were 1.76 ± 0.02 and 1.79 ± 0.02 nm, respectively. A larger $\Delta\lambda_{max}$ shift at saturation can indicate either greater surface coverage of attached vesicles or more extensive deformation of attached vesicles,[46,47] which led us to further investigate the corresponding attachment kinetics.

More specifically, we evaluated the initial rate of change in the $\Delta\lambda_{max}$ signal, which depends on the rate of diffusion-limited vesicle attachment[48] and the extent of attached vesicle deformation[43,49] (Figure 2C). Because the vesicle diameter was measured to be ∼70 nm by dynamic light-scattering experiments in all cases and all other experimental parameters were fixed, the vesicle attachment rate was constant. Hence, a larger rate of change in the $\Delta\lambda_{max}$ signal corresponded to greater deformation of attached vesicles.[37] Accordingly, we determined that the initial rate of change in the $\Delta\lambda_{max}$ signal

https://doi.org/10.1021/acs.jpclett.1c01510
J. Phys. Chem. Lett. 2021, 12, 6722−6729

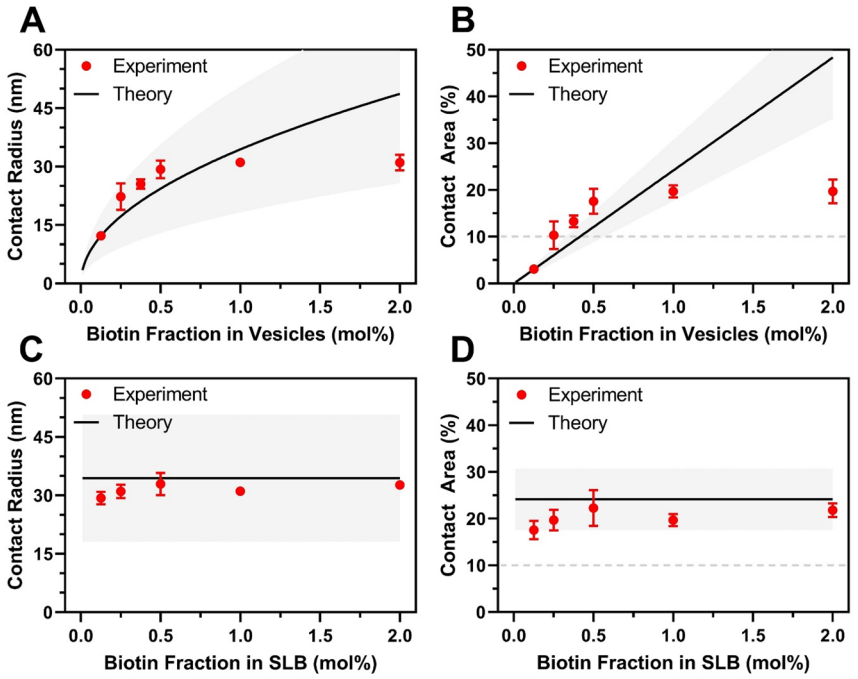

Figure 4. Deformation of attached vesicles from LSPR data analysis and theoretical comparison. (A) Radius of the vesicle−SLB contact region and (B) percentage of total vesicle surface area that contacts the SLB when the biotin fraction in the vesicles was varied from 0.25 to 2 mol % and the biotin fraction in the SLB was fixed at 1 mol %. (C and D) Corresponding data when the biotin fraction in the SLB was varied from 0.125 to 2 mol % and the biotin fraction in the vesicles was fixed at 1 mol %. Red circles and black lines represent the radii that were determined from analyzing LSPR experimental data (see eq 2) and from theoretical calculations that assumed fully flexible vesicles, respectively (see eqs 3 and 4 for panels A/C and B/D, respectively). Dashed gray lines correspond to the onset of appreciable vesicle deformation for ≥10% contact area, whereas shaded gray regions represent the uncertainty in the theoretical calculations. All data are reported as the mean ± standard deviation from three measurement runs.

(defined as the maximum slope value) was 0.16 ± 0.02 nm/min for vesicles with 0.125 mol % biotin. For vesicles with 0.25 and 0.375 mol % biotin, the initial rates of change in the $\Delta\lambda_{max}$ signal were 0.24 ± 0.02 and 0.26 ± 0.01 nm/min, respectively, and the rate increased to 0.29 ± 0.02 nm/min for vesicles with 0.5 mol % biotin. Appreciably larger initial rates of change in the $\Delta\lambda_{max}$ signal of 0.31 ± 0.01 and 0.31 ± 0.02 nm/min were observed for vesicles with 1 and 2 mol % biotin, respectively. These findings support that the deformation of attached vesicles tended to be greater for vesicles with larger biotin fractions up to a certain point. For vesicles with ≥1 mol % biotin fractions, the similar, experimentally tracked rates suggest that the extent of attached vesicle deformation remains roughly the same within this range.

While this analysis focuses on scrutinizing the deformation of attached vesicles in the low surface coverage regime, the trend in the rates of change largely mirrors the trend in $\Delta\lambda_{max}$ shifts at saturation as described above. Considering that the extent of attached vesicle deformation is mainly affected by vesicle−SLB interactions, the similar trends further support that, with increasing biotin fraction in the vesicles, the larger $\Delta\lambda_{max}$ shifts at saturation also occur due to greater deformation of attached vesicles.

In addition to changing the biotin fraction in vesicles, Figure 3A presents the time-resolved $\Delta\lambda_{max}$ shifts for tracking vesicle attachment onto streptavidin-functionalized SLBs with variable biotin fractions (0.125−2 mol %) and a fixed biotin fraction (1 mol %) in the vesicles. Monotonic attachment until saturation was again observed, and the final $\Delta\lambda_{max}$ shifts were generally larger for vesicle attachment onto SLBs with greater biotin fractions. For SLBs with 0.125 and 0.25 mol % biotin, the final $\Delta\lambda_{max}$ shifts at saturation were 0.60 ± 0.01 and 0.93 ± 0.02 nm, respectively, while the $\Delta\lambda_{max}$ shift markedly increased to 1.51 ± 0.04 nm for SLBs with 0.5 mol % biotin (Figure 3B). On the other hand, for SLBs with 1 and 2 mol % biotin, the corresponding $\Delta\lambda_{max}$ shifts were 1.76 ± 0.02 and 1.91 ± 0.02 nm, respectively.

We also evaluated the initial rate of change in the $\Delta\lambda_{max}$ signal for all cases and, in marked contrast to the first experimental series, observed nearly negligible rate changes as a function of biotin fraction in the SLB (Figure 3C). The initial rate of change in the $\Delta\lambda_{max}$ signal was 0.29 ± 0.01 nm/min for vesicle attachment onto SLBs with 0.0125 mol % biotin, while the rates slightly increased to 0.31 ± 0.01 and 0.33 ± 0.03 nm/min for SLBs with 0.25 and 0.5 mol % biotin, respectively. Similar rates of 0.31 ± 0.01 and 0.33 ± 0.01 nm/min were recorded for vesicle attachment onto SLBs with 1 and 2 mol % biotin, respectively. These results indicate that the extent of attached vesicle deformation is similar in all cases and that the dependence of the final $\Delta\lambda_{max}$ shift on the biotin fraction in the SLB is related to the surface coverage of attached vesicles at saturation. We also verified the experimentally observed trends in vesicle attachment kinetics by conducting QCM-D measurements, which showed qualitative agreement with the LSPR data (Figures S5 and S6). Collectively, the findings support that varying the biotin fraction in the vesicles modulates the degree of attached vesicle deformation while varying the biotin fraction in the SLB influences the surface coverage of attached vesicles but does not affect the extent of vesicle deformation.

As mentioned above, the vesicle attachment kinetics under consideration exhibit the transient, nearly linear regime and

https://doi.org/10.1021/acs.jpclett.1c01510
J. Phys. Chem. Lett. 2021, 12, 6722−6729

subsequent steady state (see also section 2 in the Supporting Information). Our theoretical estimates indicate that formation of the vesicle−SLB contact region, including redistribution of biotinylated lipids, occurs rapidly just after attachment of a vesicle (section 3 in the Supporting Information), and the size of this region is determined primarily by the number of biotinylated lipids in a vesicle, which is expected to affect the extent of attached vesicle deformation.

To interpret the LSPR measurement data, we scrutinized the linear phase of the corresponding attachment kinetics and extracted the radius of the vesicle−SLB contact region (section 4 in the Supporting Information). We recall that the corresponding LSPR penetration length, a, is relatively short and note that the dependence of the LSPR signal on the vesicle geometry can be calculated analytically by using the dipole attenuation function, ${R_*}^6/(R_* + z)^6$ (refs 50 and 51), where R_* is the effective radius of plasmonic nanodisks (in this model, $a = R_*/5$). Deformed vesicles can be represented by a truncated sphere with a flat basement of radius r. In our case, the extent of vesicle deformation is weak or relatively modest and the radius of the truncated sphere is close to that of vesicles in solution, R = 35 nm. Under this condition, the LSPR signal is proportional in good approximation to $2aR + r^2$ (see refs 50 and 51 and eq 11 in the Supporting Information).

Taking into account the diffusion-limited vesicle adsorption kinetics in the linear regime, the LSPR measurement response can be described as

$$\Delta\lambda_{max} = B(2aR + r^2)C_v t \tag{1}$$

where B is a constant that depends on the measurement specifics (i.e., on flow channel dimensions and sensor sensitivity), C_v is the vesicle concentration in solution, and t is time. With increasing biotin fraction in vesicles, as already noticed, r is expected to increase and the $\Delta\lambda_{max}$ shift should increase as well. Because t corresponds to the time from which vesicle attachment commenced, eq 1 can be rewritten as

$$\frac{\Delta\lambda_{max}}{\Delta t} \simeq \frac{d\lambda_{max}}{dt} = B(2aR + r^2)C_v \tag{2}$$

In this equation, the initial rate of change in the LSPR signal during each measurement run is measured, whereas all other values except the radius of the vesicle−SLB contact region, r, can be calculated or are known from independent measurements (see sections 1, 2, and 4 in the Supporting Information), and accordingly the value of r can be determined from each LSPR measurement run.

When the biotin fraction in the SLB was fixed at 1 mol % and the biotin fraction in vesicles was varied from 0.125 to 2 mol %, the radius of the contact region increased from ∼12 nm to 30 ± 2 nm (Figure 4A). At relatively low biotin fractions in the vesicles, the experimental results agreed well with theoretical estimates assuming maximum deformation of a fully flexible vesicle and that all of the biotinylated lipids in the outer leaflet of a vesicle are located in the contact region and form biotin−streptavidin complexes (BSCs) (section 5 in the Supporting Information). Specifically, the theoretical estimate was obtained by calculating the maximal radius of the vesicle−SLB contact region, r_{max}, as follows:

$$r_{max} = \left(\frac{2R^2\chi_v s_s}{s_l}\right)^{1/2} \tag{3}$$

where χ_v is the biotin fraction in a vesicle, s_s the area per streptavidin (≅29 nm^2), and s_l the area per lipid (≅0.6 nm^2). On the other hand, at higher biotin fractions (>1 mol %), there was a larger gap between the experimental results and theoretical prediction.

From the radius of the vesicle−SLB contact region, we also calculated the percentage of the total vesicle surface area, $4\pi R^2$, that contacts the SLB, πr^2, and this percentage increased from ∼3% to 20 ± 2% when the biotin fraction in vesicles was varied from 0.125 to 2 mol % (Figure 4B). Previous studies[23,34] have defined vesicle deformation as appreciable when this percentage value exceeds 10%, which corresponds to an equivalent biotin fraction of 0.27 mol % for the vesicles in our experiments based on linear regression analysis. According to the theoretical analyses, the contact area, S_{max}, of an attached vesicle was also calculated as

$$S_{max} = \frac{2\pi R^2\chi_v s_s}{s_l} \tag{4}$$

and applied to theoretically estimate the contact area percentage as a function of biotin fraction. On the basis of these results, the trends in experimental values and theoretical estimates agreed well for vesicles with 0.125−1 mol % biotin while there was a deviation for vesicles with 2 mol % biotin. The latter result supports that the extent of vesicle deformation is partially counterposed by the need to increase the vesicle bending energy.

On the other hand, when the biotin fraction in vesicles was fixed at 1 mol % and the biotin fraction in the SLB was varied from 0.125 to 2 mol %, the radius of the contact region was nearly constant around 31 nm (Figure 4C). This trend agreed well with the trend predicted by theoretical calculations based on a fully flexible vesicle and is in line with eq 3, which does not depend on the biotin fraction in the SLB. The corresponding percentage of the vesicle surface area that contacted the SLB was around 20% in all cases, which indicates appreciable deformation and is in line with eq 4 that also does not depend on the biotin fraction in the SLB (Figure 4D).

Considering the LSPR data, we can further estimate the membrane bending energy of the vesicles in our experiments by taking into account that the onset of appreciable deformation occurs for vesicles with 0.27 mol % biotin (equivalent to f = 0.0027, where f is the molar fraction of biotinylated lipids in a vesicle). Indeed, the BSC-induced deformation of an attached vesicle is partly counterposed by the need to deform a vesicle or, more specifically, by the corresponding membrane bending energy (section 6 in the Supporting Information). Our theoretical analysis supports that, when $f \leq 0.0027$, the number of biotins (on the vesicle side) involved in the vesicle−SLB contact region is ≤69. The formation of biotin−streptavidin pairs in the contact region is accompanied by the loss of entropy of biotinylated lipids and streptavidin proteins, which can be estimated as $-2k_BT \ln(f)$ or 5.9 kcal/mol (when f = 0.0027). The Gibbs free energy, ΔG, of biotin−streptavidin binding is around 18 kcal/mol (ref 52), so the free energy gain due to bond formation is around 18 − 5.9 = 12.1 kcal/mol per pair. For 69 pairs, this gain is around 800 kcal/mol or 1400 k_BT, from which it can be determined that the membrane bending rigidity, κ, of the attached vesicles is about 700 k_BT because the vesicle bending energy is comparable with 2κ for modest vesicle deformations (see analysis in ref 23), and this value fits within the range of

https://doi.org/10.1021/acs.jpclett.1c01510
J. Phys. Chem. Lett. 2021, 12, 6722−6729

literature estimates for sub-100 nm lipid vesicles.[23,37,53] As such, this finding reinforces that the LSPR measurement approach taken here is useful for extracting structural and energetic information about biological nanoparticles, in this case lipid vesicles, that bind multivalently to receptor-functionalized surfaces.

To contextualize these findings, we briefly discuss recent trends in the field. Many studies have investigated the receptor-mediated attachment of biological nanoparticles to biomimetic and biological surfaces, and the main focus has been on scrutinizing the attachment process while treating the biological nanoparticles as nondeformable in most cases. In a few cases,[21,22] there has been discussion about the possible deformation of biological nanoparticles (exosomes) by conducting conventional SPR experiments, but the penetration depth of the SPR technique is typically greater than 100 nm,[54] which means that it has relatively low sensitivity to nanoparticle shape changes that occur near the sensor surface. Using the attachment of biotinylated lipid vesicles to a streptavidin-functionalized SLB as a model system, our findings demonstrate that the high surface sensitivity of the LSPR technique is advantageous to track receptor-mediated vesicle attachment and corresponding shape changes, especially in combination with a newly developed analytical model to extract quantitative information about the vesicle−SLB contact region. From a physicochemical perspective, our theoretical analyses take into account various factors, such as redistribution of BSCs and biotinylated lipids, multivalent biotin−streptavidin binding interactions, and vesicle bending energy. The interplay of the corresponding concepts and equations provides fundamental insight into structural and energetic aspects of receptor-mediated vesicle deformation.

The conceptual framework and tools developed in this study can be broadly useful to investigate a wide range of fundamental and applied topics related to the attachment and subsequent reshaping of biological and biomimetic nanoparticles. Among various possibilities, one option involves studying the attachment and deformation of membrane-enveloped virions that bind to membrane-associated cell surface receptors and testing antiviral drug candidates that decrease the fluidity of viral membranes[55] to potentially inhibit receptor-mediated deformation.

■ ASSOCIATED CONTENT

Supporting Information

The Supporting Information is available free of charge at https://pubs.acs.org/doi/10.1021/acs.jpclett.1c01510.

Experimental details, vesicle attachment kinetics, redistribution of BSCs and biotinylated lipids, vesicle deformation analysis from LSPR data, structural and energetic aspects of vesicle deformation, and additional QCM-D data (Figures S1−S6) (PDF)

■ AUTHOR INFORMATION

Corresponding Authors

Nam-Joon Cho − *School of Materials Science and Engineering, Nanyang Technological University, 637553, Singapore;* orcid.org/0000-0002-8692-8955; Email: njcho@ntu.edu.sg

Joshua A. Jackman − *School of Chemical Engineering, Sungkyunkwan University, Suwon 16419, Republic of Korea;* orcid.org/0000-0002-1800-8102; Email: jjackman@skku.edu

Authors

Hyeonjin Park − *School of Chemical Engineering, Sungkyunkwan University, Suwon 16419, Republic of Korea; School of Materials Science and Engineering, Nanyang Technological University, 637553, Singapore*

Tun Naw Sut − *School of Chemical Engineering, Sungkyunkwan University, Suwon 16419, Republic of Korea; School of Materials Science and Engineering, Nanyang Technological University, 637553, Singapore*

Bo Kyeong Yoon − *School of Chemical Engineering, Sungkyunkwan University, Suwon 16419, Republic of Korea*

Vladimir P. Zhdanov − *Boreskov Institute of Catalysis, Russian Academy of Sciences, Novosibirsk 630090, Russia;* orcid.org/0000-0002-0167-8783

Complete contact information is available at: https://pubs.acs.org/10.1021/acs.jpclett.1c01510

Author Contributions

§H.P. and T.N.S. contributed equally to this work.

Notes

The authors declare no competing financial interest.

■ ACKNOWLEDGMENTS

This work was supported by the National Research Foundation of Korea (NRF) grants funded by the Korean government (MSIT) (Nos. 2020R1C1C1004385 and 2021R1A4A1032782). In addition, this work was supported by the Brain Pool Program through the National Research Foundation of Korea (NRF) funded by the Ministry of Science and ICT (2019H1D3A1A01070318).

■ ABBREVIATIONS

BSC:biotin−streptavidin complex
DOPC:1,2-dioleoyl-*sn*-glycero-3-phosphocholine
DOPE-biotin:1,2-dioleoyl-*sn*-glycero-3-phosphoethanolamine-N-(cap biotinyl)
LSPR:localized surface plasmon resonance
QCM-D:quartz crystal microbalance-dissipation
SLB:supported lipid bilayer

■ REFERENCES

(1) Mammen, M.; Choi, S. K.; Whitesides, G. M. Polyvalent Interactions in Biological Systems: Implications for Design and Use of Multivalent Ligands and Inhibitors. *Angew. Chem., Int. Ed.* **1998**, *37*, 2754−2794.

(2) Fasting, C.; Schalley, C. A.; Weber, M.; Seitz, O.; Hecht, S.; Koksch, B.; Dernedde, J.; Graf, C.; Knapp, E. W.; Haag, R. Multivalency as a Chemical Organization and Action Principle. *Angew. Chem., Int. Ed.* **2012**, *51*, 10472−10498.

(3) Cawley, J. L.; Jordan, L. R.; Wittenberg, N. J. Detection and Characterization of Vesicular Gangliosides Binding to Myelin-Associated Glycoprotein on Supported Lipid Bilayers. *Anal. Chem.* **2021**, *93*, 1185−1192.

(4) Junesch, J.; Emilsson, G.; Xiong, K.; Kumar, S.; Sannomiya, T.; Pace, H.; Vörös, J.; Oh, S.-H.; Bally, M.; Dahlin, A. B. Location-Specific Nanoplasmonic Sensing of Biomolecular Binding to Lipid Membranes with Negative Curvature. *Nanoscale* **2015**, *7*, 15080−15085.

(5) Nakase, I.; Ueno, N.; Katayama, M.; Noguchi, K.; Takatani-Nakase, T.; Kobayashi, N. B.; Yoshida, T.; Fujii, I.; Futaki, S. Receptor Clustering and Activation by Multivalent Interaction through

Recognition Peptides Presented on Exosomes. *Chem. Commun.* **2017**, *53*, 317−320.
(6) Müller, M.; Lauster, D.; Wildenauer, H. H.; Herrmann, A.; Block, S. Mobility-Based Quantification of Multivalent Virus-Receptor Interactions: New Insights into Influenza A Virus Binding Mode. *Nano Lett.* **2019**, *19*, 1875−1882.
(7) Koehler, M.; Delguste, M.; Sieben, C.; Gillet, L.; Alsteens, D. Initial Step of Virus Entry: Virion Binding to Cell-Surface Glycans. *Annu. Rev. Virol.* **2020**, *7*, 143−165.
(8) Overeem, N. J.; van der Vries, E.; Huskens, J. A Dynamic, Supramolecular View on the Multivalent Interaction between Influenza Virus and Host Cell. *Small* **2021**, *17*, 2007214.
(9) Zhdanov, V. P. Virology from the Perspective of Theoretical Colloid and Interface Science. *Curr. Opin. Colloid Interface Sci.* **2021**, *53*, 101450.
(10) Srinivasan, A.; Viswanathan, K.; Raman, R.; Chandrasekaran, A.; Raguram, S.; Tumpey, T. M.; Sasisekharan, V.; Sasisekharan, R. Quantitative Biochemical Rationale for Differences in Transmissibility of 1918 Pandemic Influenza A Viruses. *Proc. Natl. Acad. Sci. U. S. A.* **2008**, *105*, 2800−2805.
(11) Thompson, A. J.; Paulson, J. C. Adaptation of Influenza Viruses to Human Airway Receptors. *J. Biol. Chem.* **2021**, *296*, 100017.
(12) Komiyama, M.; Yoshimoto, K.; Sisido, M.; Ariga, K. Chemistry Can Make Strict and Fuzzy Controls for Bio-Systems: DNA Nanoarchitectonics and Cell-Macromolecular Nanoarchitectonics. *Bull. Chem. Soc. Jpn.* **2017**, *90*, 967−1004.
(13) Cheng, Q.; Shi, X.; Han, M.; Smbatyan, G.; Lenz, H.-J.; Zhang, Y. Reprogramming Exosomes as Nanoscale Controllers of Cellular Immunity. *J. Am. Chem. Soc.* **2018**, *140*, 16413−16417.
(14) Woythe, L.; Tito, N. B.; Albertazzi, L. A Quantitative View on Multivalent Nanomedicine Targeting. *Adv. Drug Delivery Rev.* **2021**, *169*, 1−12.
(15) Poellmann, M. J.; Nair, A.; Bu, J.; Kim, J. K.; Kimple, R. J.; Hong, S. Immunoavidity-Based Capture of Tumor Exosomes Using Poly(amidoamine) Dendrimer Surfaces. *Nano Lett.* **2020**, *20*, 5686−5692.
(16) Nie, C.; Stadtmüller, M.; Parshad, B.; Wallert, M.; Ahmadi, V.; Kerkhoff, Y.; Bhatia, S.; Block, S.; Cheng, C.; Wolff, T.; et al. Heteromultivalent Topology-Matched Nanostructures as Potent and Broad-Spectrum Influenza A Virus Inhibitors. *Sci. Adv.* **2021**, *7*, No. eabd3803.
(17) Parveen, N.; Rydell, G. E.; Larson, G.; Hytönen, V. P.; Zhdanov, V. P.; Höök, F.; Block, S. Competition for Membrane Receptors: Norovirus Detachment via Lectin Attachment. *J. Am. Chem. Soc.* **2019**, *141*, 16303−16311.
(18) Di Iorio, D.; Verheijden, M. L.; Van Der Vries, E.; Jonkheijm, P.; Huskens, J. Weak Multivalent Binding of Influenza Hemagglutinin Nanoparticles at a Sialoglycan-Functionalized Supported Lipid Bilayer. *ACS Nano* **2019**, *13*, 3413−3423.
(19) Overeem, N. J.; Hamming, P. E.; Grant, O. C.; Di Iorio, D.; Tieke, M.; Bertolino, M. C.; Li, Z.; Vos, G. l.; De Vries, R. P.; Woods, R. J.; et al. Hierarchical Multivalent Effects Control Influenza Host Specificity. *ACS Cent. Sci.* **2020**, *6*, 2311−2318.
(20) Scheepers, M.; van IJzendoorn, L.; Prins, M. Multivalent Weak Interactions Enhance Selectivity of Interparticle Binding. *Proc. Natl. Acad. Sci. U. S. A.* **2020**, *117*, 22690−22697.
(21) Rupert, D. L. M.; Lässer, C.; Eldh, M.; Block, S.; Zhdanov, V. P.; Lotvall, J. O.; Bally, M.; Höök, F. Determination of Exosome Concentration in Solution Using Surface Plasmon Resonance Spectroscopy. *Anal. Chem.* **2014**, *86*, 5929−5936.
(22) Rupert, D. L. M.; Shelke, G. V.; Emilsson, G.; Claudio, V.; Block, S.; Lässer, C.; Dahlin, A.; Lötvall, J. O.; Bally, M.; Zhdanov, V. P.; Höök, F. Dual-Wavelength Surface Plasmon Resonance for Determining the Size and Concentration of Sub-Populations of Extracellular Vesicles. *Anal. Chem.* **2016**, *88*, 9980−9988.
(23) Zhdanov, V. P. Ligand-Receptor-Mediated Attachment of Lipid Vesicles to a Supported Lipid Bilayer. *Eur. Biophys. J.* **2020**, *49*, 395−400.
(24) Zhdanov, V. P. Competitive Multivalent Coadsorption and Desorption of Biological Nanoparticles on a Supported Lipid Bilayer. *Chem. Phys. Lett.* **2020**, *750*, 137468.
(25) Sun, S. X.; Wirtz, D. Mechanics of Enveloped Virus Entry into Host Cells. *Biophys. J.* **2006**, *90*, L10−L12.
(26) Li, L.; Liu, X.; Zhou, Y.; Wang, J. On Resistance to Virus Entry into Host Cells. *Biophys. J.* **2012**, *102*, 2230−2233.
(27) Zhdanov, V. P. Physical Aspects of the Initial Phase of Endocytosis. *Phys. Rev. E* **2013**, *88*, No. 064701.
(28) Zhdanov, V. P. Kinetics of Virus Entry by Endocytosis. *Phys. Rev. E* **2015**, *91*, No. 042715.
(29) Frey, F.; Ziebert, F.; Schwarz, U. S. Stochastic Dynamics of Nanoparticle and Virus Uptake. *Phys. Rev. Lett.* **2019**, *122*, No. 088102.
(30) Zhdanov, V. P. Multivalent Ligand-Receptor-Mediated Interaction of Small Filled Vesicles with a Cellular Membrane. *Phys. Rev. E: Stat. Phys., Plasmas, Fluids, Relat. Interdiscip. Top.* **2017**, *96*, No. 012408.
(31) Ewers, H.; Römer, W.; Smith, A. E.; Bacia, K.; Dmitrieff, S.; Chai, W.; Mancini, R.; Kartenbeck, J.; Chambon, V.; Berland, L.; Oppenheim, A.; Schwarzmann, G.; Feizi, T.; Schwille, P.; Sens, P.; Helenius, A.; Johannes, L. GM1 Structure Determines SV40-Induced Membrane Invagination and Infection. *Nat. Cell Biol.* **2010**, *12*, 11−18.
(32) Arnaud, J.; Tröndle, K.; Claudinon, J.; Audfray, A.; Varrot, A.; Römer, W.; Imberty, A. Membrane Deformation by Neolectins with Engineered Glycolipid Binding Sites. *Angew. Chem.* **2014**, *126*, 9421−9424.
(33) Parveen, N.; Rimkute, I.; Block, S.; Rydell, G. E.; Midtvedt, D.; Larson, G.; Hytönen, V. P.; Zhdanov, V. P.; Lundgren, A.; Höök, F. Membrane Deformation Induces Clustering of Norovirus Bound to Glycosphingolipids in a Supported Cell-Membrane Mimic. *J. Phys. Chem. Lett.* **2018**, *9*, 2278−2284.
(34) Di Iorio, D.; Lu, Y.; Meulman, J.; Huskens, J. Recruitment of Receptors at Supported Lipid Bilayers Promoted by the Multivalent Binding of Ligand-Modified Unilamellar Vesicles. *Chem. Sci.* **2020**, *11*, 3307−3315.
(35) Mapar, M.; Jõemetsa, S.; Pace, H.; Zhdanov, V. P.; Agnarsson, B.; Höök, F. Spatiotemporal Kinetics of Supported Lipid Bilayer Formation on Glass via Vesicle Adsorption and Rupture. *J. Phys. Chem. Lett.* **2018**, *9*, 5143−5149.
(36) Yoon, B. K.; Park, S.; Ma, G. J.; Kolahdouzan, K.; Zhdanov, V. P.; Jackman, J. A.; Cho, N.-J. Competing Interactions of Fatty Acids and Monoglycerides Trigger Synergistic Phospholipid Membrane Remodeling. *J. Phys. Chem. Lett.* **2020**, *11*, 4951−4957.
(37) Jackman, J. A.; Yorulmaz Avsar, S.; Ferhan, A. R.; Li, D.; Park, J. H.; Zhdanov, V. P.; Cho, N.-J. Quantitative Profiling of Nanoscale Liposome Deformation by a Localized Surface Plasmon Resonance Sensor. *Anal. Chem.* **2017**, *89*, 1102−1109.
(38) Ridolfi, A.; Brucale, M.; Montis, C.; Caselli, L.; Paolini, L.; Borup, A.; Boysen, A. T.; Loria, F.; van Herwijnen, M. J. C.; Kleinjan, M.; Nejsum, P.; Zarovni, N.; Wauben, M. H. M.; Berti, D.; Bergese, P.; Valle, F. AFM-Based High-Throughput Nanomechanical Screening of Single Extracellular Vesicles. *Anal. Chem.* **2020**, *92*, 10274−10282.
(39) Jackman, J. A.; Ferhan, A. R.; Cho, N.-J. Nanoplasmonic Sensors for Biointerfacial Science. *Chem. Soc. Rev.* **2017**, *46*, 3615−3660.
(40) Willets, K. A.; Van Duyne, R. P. Localized Surface Plasmon Resonance Spectroscopy and Sensing. *Annu. Rev. Phys. Chem.* **2007**, *58*, 267−297.
(41) Larsson, E. M.; Edvardsson, M. E.; Langhammer, C.; Zorić, I.; Kasemo, B. A Combined Nanoplasmonic and Electrodeless Quartz Crystal Microbalance Setup. *Rev. Sci. Instrum.* **2009**, *80*, 125105.
(42) Park, H.; Ma, G. J.; Yoon, B. K.; Cho, N.-J.; Jackman, J. A. Comparing Protein Adsorption onto Alumina and Silica Nanomaterial Surfaces: Clues for Vaccine Adjuvant Development. *Langmuir* **2021**, *37*, 1306−1314.

https://doi.org/10.1021/acs.jpclett.1c01510
J. Phys. Chem. Lett. 2021, 12, 6722−6729

(43) Zan, G. H.; Jackman, J. A.; Kim, S. O.; Cho, N. J. Controlling Lipid Membrane Architecture for Tunable Nanoplasmonic Biosensing. *Small* **2014**, *10*, 4828−4832.
(44) Jackman, J. A.; Cho, N.-J. Supported Lipid Bilayer Formation: Beyond Vesicle Fusion. *Langmuir* **2020**, *36*, 1387−1400.
(45) Rodrigo, D.; Tittl, A.; Ait-Bouziad, N.; John-Herpin, A.; Limaj, O.; Kelly, C.; Yoo, D.; Wittenberg, N. J.; Oh, S.-H.; Lashuel, H. A.; Altug, H. Resolving Molecule-Specific Information in Dynamic Lipid Membrane Processes with Multi-Resonant Infrared Metasurfaces. *Nat. Commun.* **2018**, *9*, 2160.
(46) Oh, E.; Jackman, J. A.; Yorulmaz, S.; Zhdanov, V. P.; Lee, H.; Cho, N.-J. Contribution of Temperature to Deformation of Adsorbed Vesicles Studied by Nanoplasmonic Biosensing. *Langmuir* **2015**, *31*, 771−781.
(47) Dacic, M.; Jackman, J. A.; Yorulmaz, S.; Zhdanov, V. P.; Kasemo, B.; Cho, N.-J. Influence of Divalent Cations on Deformation and Rupture of Adsorbed Lipid Vesicles. *Langmuir* **2016**, *32*, 6486−6495.
(48) Zhdanov, V.; Keller, C.; Glasmästar, K.; Kasemo, B. Simulation of Adsorption Kinetics of Lipid Vesicles. *J. Chem. Phys.* **2000**, *112*, 900−909.
(49) Jackman, J. A.; Špačková, B.; Linardy, E.; Kim, M. C.; Yoon, B. K.; Homola, J.; Cho, N.-J. Nanoplasmonic Ruler to Measure Lipid Vesicle Deformation. *Chem. Commun.* **2016**, *52*, 76−79.
(50) Jackman, J. A.; Zhdanov, V. P.; Cho, N.-J. Nanoplasmonic Biosensing for Soft Matter Adsorption: Kinetics of Lipid Vesicle Attachment and Shape Deformation. *Langmuir* **2014**, *30*, 9494−9503.
(51) Yoon, B. K.; Park, H.; Zhdanov, V. P.; Jackman, J. A.; Cho, N.-J. Real-Time Nanoplasmonic Sensing of Three-Dimensional Morphological Changes in a Supported Lipid Bilayer and Antimicrobial Testing Applications. *Biosens. Bioelectron.* **2021**, *174*, 112768.
(52) Weber, P.; Wendoloski, J.; Pantoliano, M.; Salemme, F. Crystallographic and Thermodynamic Comparison of Natural and Synthetic Ligands Bound to Streptavidin. *J. Am. Chem. Soc.* **1992**, *114*, 3197−3200.
(53) Takechi-Haraya, Y.; Sakai-Kato, K.; Abe, Y.; Kawanishi, T.; Okuda, H.; Goda, Y. Atomic Force Microscopic Analysis of the Effect of Lipid Composition on Liposome Membrane Rigidity. *Langmuir* **2016**, *32*, 6074−6082.
(54) Homola, J. Surface Plasmon Resonance Sensors for Detection of Chemical and Biological Species. *Chem. Rev.* **2008**, *108*, 462−493.
(55) Vigant, F.; Santos, N. C.; Lee, B. Broad-Spectrum Antivirals against Viral Fusion. *Nat. Rev. Microbiol.* **2015**, *13*, 426−437.

https://doi.org/10.1021/acs.jpclett.1c01510
J. Phys. Chem. Lett. 2021, 12, 6722−6729